SCIENCE CHINA
Chemistry

•ARTICLES•

June 2025 Vol.68 No.6: 2424–2432
https://doi.org/10.1007/s11426-024-2391-0

In-situ synthesis of layered double hydroxides with tunable basal spacing for efficient iodide over iodate adsorption selectivity

Xiaolu Liu[1†], Muliang Xiao[1†], Pei Chen[1], Yilun Zhou[1], Yinghui Xie[1], Mengjie Hao[1], Liang Mao[2], Hui Yang[1*], Geoffrey I. N. Waterhouse[3], Shengqian Ma[4*] & Xiangke Wang[1*]

[1]*College of Environmental Science and Engineering, North China Electric Power University, Beijing 102206, China*
[2]*State Key Laboratory of Pollution Control and Resource Reuse, School of the Environment, Nanjing University, Nanjing 210093, China*
[3]*School of Chemical Sciences, the University of Auckland, Auckland 1142, New Zealand*
[4]*Department of Chemistry, University of North Texas, Denton, TX 76201, USA*

Received September 19, 2024; accepted October 29, 2024; published online November 5, 2024

Separating I_3^- and IO_3^- from aqueous solutions is technically challenging due to their very similar charge density. Herein, we describe the *in-situ* synthesis of cobalt-based layered double hydroxides (Co-LDHs) by decomposition of zeolite imidazole framework (ZIF) nanocrystals, whilst modulating the basal spacing in the Co-LDHs through anion intercalation (such as Br^-, NO_3^-, and ClO_4^-). Co-LDH-NO_3^- possesses an optimal basal spacing of ~4.69 Å, which is slightly smaller than the van der Waals diameter of IO_3^- (~4.79 Å), thus enabling selective adsorption of linear I_3^- (diameter ~4.22 Å) *via* ion exchange in the LDH interlayer. Co-LDH-NO_3^- showed ultrafast I_3^- uptake kinetics involving strong "host-guest" interaction forces, achieving high dynamic uptake capacities of 119.94 and 127.18 mg/g in I_3^-/IO_3^- contaminated groundwater and tap water, respectively, and ~100% separation efficiencies towards I_3^- over IO_3^-. Co-LDH-Br^- with a smaller basal spacing (4.06 Å) exhibited much slower separation kinetics, and Co-LDH-ClO_4^- with a ~5.36 Å basal spacing demonstrated poor separation efficiency under similar conditions. *Ab initio* molecular dynamics (AIMD) simulations were used to visually simulate the ion exchange process, with the results being consistent with the experimental observations. Furthermore, Co-LDH-NO_3^- demonstrated excellent reusability during dynamic breakthrough tests and I_3^-/IO_3^- separation cycles due to a "special memory effect" of the 2D interlayer. This work guides adsorbent design for the efficient removal and separation of iodine species from contaminated water.

I_3^-/IO_3^- separation, layered double hydroxides, tunable basal spacing, Co-LDH-NO_3^-, environmental management

Citation: Liu X, Xiao M, Chen P, Zhou Y, Xie Y, Hao M, Mao L, Yang H, Waterhouse GIN, Ma S, Wang X. *In-situ* synthesis of layered double hydroxides with tunable basal spacing for efficient iodide over iodate adsorption selectivity. *Sci China Chem*, 2025, 68: 2424–2432, https://doi.org/10.1007/s11426-024-2391-0

1 Introduction

Iodine is a trace element widely present in natural water systems. As such, it does not typically pose a threat to human health and the ecological environment in the natural state [1–4]. However, human activities, including industrial emissions, agricultural runoff, radioactive iodine production in nuclear reactors, *etc*., can all cause iodine contamination in natural water sources [5–13]. Specifically, iodine that enters the body in excess through the aqueous environment increases the risk of thyroid abnormalities or acute poisoning in humans [14–21]. Additionally, high concentrations of iodine in natural water can be toxic to aquatic organisms, potentially threatening aquatic ecosystems and biodiversity and ultimately endangering human health through the food chain [22–24]. Therefore, effectively controlling and reducing iodine pollution in the water and the wider environment is of

†Equally contributed to this work.
*Corresponding authors (email: h.yang@ncepu.edu.cn; shengqian.ma@unt.edu; xkwang@ncepu.edu.cn)

great importance for public health and ecological protection.

Iodine pollutants in water primarily exist in the form of iodide ($I_2+I^- \rightleftharpoons I_3^-$) and iodate ($IO_3^-$) [25–27]. The separation of these two forms of iodine in water is crucial for accurately assessing the extent of iodine pollution and identifying its sources, thereby providing more precise information for environmental monitoring [28,29]. Moreover, by assessing the toxicity and bioavailability of iodide and iodate ions, the health status of aquatic ecosystems can be determined, and potential ecological risks can be predicted/mitigated [30,31]. Consequentially, high-efficiency separation of I_3^- and IO_3^- in water bodies is crucial for iodine pollution control, thereby reducing iodine hazards to the environment and human health.

Since IO_3^- and I_3^- possess the same charge density and high water solubility, the effective separation of I_3^- and IO_3^- from aqueous solution is challenging [32,33]. To date, sorbents such as activated carbon [34,35], metal oxides [36], silver-based nanostructures [37], polymers and cages [38–42], porous aromatic frameworks (PAFs) [43], metal-organic frameworks (MOFs) [23,44,45], and covalent organic frameworks (COFs) [46,47] have been reported for the removal of single iodine species (I_3^- or IO_3^-) from aqueous solutions. However, these sorbents typically show an undifferentiated affinity for both iodine species, making it difficult to efficiently separate the I_3^- and IO_3^- through adsorption or ion exchange techniques.

Considering that the van der Waals space diameter of tetrahedral IO_3^- is ~4.79 Å, while linear I_3^- has a minimum diameter of ~4.22 Å [48,49], we hypothesized a general approach for the selective adsorption of I_3^- while blocking IO_3^- adsorption through the rational design of LDH-based sorbents with well-defined basal spacings, thus achieving the efficient separation of I_3^-/IO_3^- in aqueous solutions. We first present an ion intercalation synthetic strategy based on the *in-situ* decomposition of zeolite imidazole framework (ZIF) nanocrystals for tuning the basal spacing of cobalt-based layered double hydroxides (Co-LDHs) (Figure 1a). Co-LDHs with interlayer Br^-, NO_3^- and ClO_4^- anions (denoted herein as Co-LDH-Br^-, Co-LDH-NO_3^-, and Co-LDH-ClO_4^-, respectively) gave basal spacings of ~4.06, ~4.69, and ~5.36 Å, respectively (Figure 1b). The window size of Co-LDH-Br^- and Co-LDH-NO_3^- is strictly smaller than the van der Waals diameter of IO_3^-, preventing their penetration into the interlayer of the LDHs (Figure 1c). Conversely, I_3^- can quickly diffuse into the 2D interlayer of Co-LDH-Br^- and Co-LDH-NO_3^-, being adsorbed by displacing Br^- and NO_3^-. Moreover, strong "host-guest" interaction forces between the LDH host layers and I_3^- in aqueous solution resulted in ultrafast adsorption kinetics, as was confirmed by experimental and theoretical results. As a result, Co-LDH-NO_3^- showed fast separation kinetics (reaching adsorption equilibrium in 10 s) and high capacity of 119.94 and 127.18 mg/g for I_3^- in contaminated groundwater and tap water, respectively (with ~100% separation efficiency towards I_3^-/IO_3^-). Co-LDH-Br^- with a smaller window size exhibited slower separation ki-

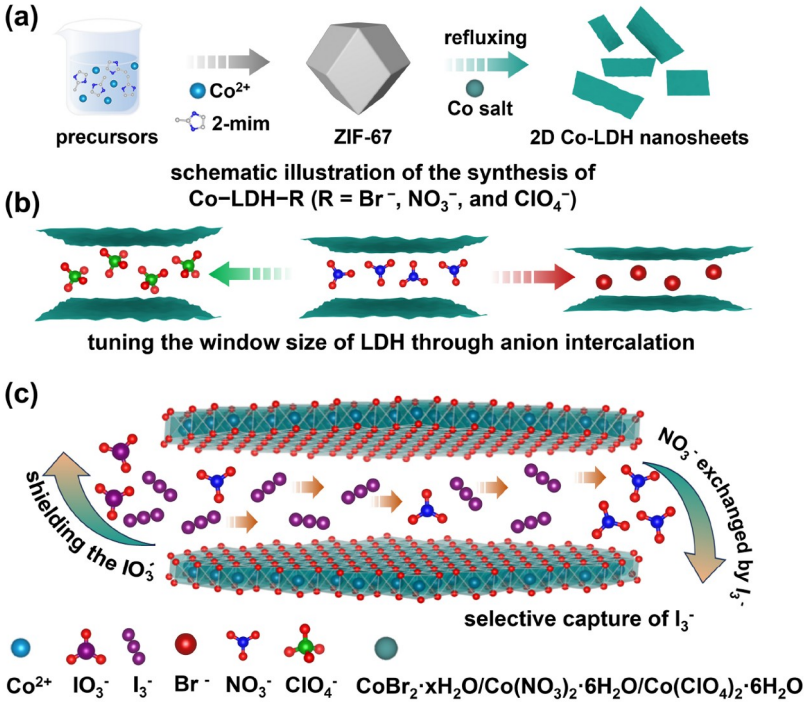

Figure 1 (Color online) (a) Schematic illustration of the synthesis of Co-LDH-R (R = Br^-, NO_3^-, and ClO_4^-). (b) Anion intercalation strategy is used to tune the basal spacing in Co-LDH-Br^-, Co-LDH-NO_3^-, and Co-LDH-ClO_4^-. (c) Schematic illustration of the separation of I_3^-/IO_3^- by Co-LDH-NO_3^-.

netics, requiring 60 min to achieve >99.9% separation efficiency. Co-LDH-ClO_4^- possessing a large interlayer channel of ~5.36 Å demonstrating poor separation efficiency under similar conditions. Breakthrough tests showed when Co-LDH-NO_3^- is used in packed columns, it can rapidly remove I_3^- from I_3^-/IO_3^- polluted groundwater and tap water with a high uptake capacity of 15.3 mg/g (>99.9% separation efficiency) and 17.6 mg/g (>99.9% separation efficiency), respectively. This study offers new vistas for the separation and capture of iodine species in contaminated water sources and aqueous solutions.

2 Experimental section

2.1 *In-situ* synthesis of Co-LDH-R (R = Br^-, NO_3^-, and ClO_4^-)

In a typical synthesis [50,51], 1 g of ZIF-67 nanocrystals were ultrasonically dispersed in a mixture of deionized water (7 mL)/ethanol (100 mL) for 30 min. Then, 4 g of $Co(NO_3)_2\cdot 6H_2O$ was added to the ZIF-67 suspension under constant stirring conditions. Next, the mixture was refluxed at 90 °C for 5 h, after which the green product was collected by filtration, and washed several times with ethanol, yielding Co-LDH-NO_3^-. The synthesis of Co-LDH-Br^- and Co-LDH-ClO_4^- were similar to that of Co-LDH-NO_3^-, except that $Co(NO_3)_2\cdot 6H_2O$ was replaced with $Co(ClO_4)_2\cdot 6H_2O$ and $CoBr_2\cdot xH_2O$, respectively.

2.2 I_3^- and IO_3^- adsorption capacity studies

The I_3^- and IO_3^- adsorption capacity experiments were carried out at 25 °C. Co-LDH-R (R = Br^-, NO_3^-, and ClO_4^-) were added into aqueous solutions with I_3^- (or IO_3^-) concentrations ranging from ~10 to ~200 ppm at a fixed adsorbent/liquid ratio of 0.4 g/L. The freshly prepared dispersions were sonicated and then shaken for 2 h. Subsequently, the dispersions were filtered on a 0.22 μm membrane filter to remove the adsorbent. After filtration, the I_3^- and IO_3^- concentrations in the filtrate were determined by UV-Vis spectroscopy at 350 nm and 200 nm, respectively.

2.3 I_3^- and IO_3^- adsorption kinetics studies

The adsorption kinetics experiments for Co-LDH-R (R = Br^-, NO_3^-, and ClO_4^-) were carried out in a mixed solution containing ~10 ppm I_3^- and ~10 ppm IO_3^- at a fixed adsorbent/liquid ratio of 0.4 g/L at 25 °C. Aliquots were collected at regular time intervals while constantly stirring the dispersion. The dispersions were filtered on a 0.22 μm membrane filter to remove the adsorbent. After filtration, the I_3^- and IO_3^- concentrations in the filtrate were determined by UV-Vis spectroscopy at 350 and 200 nm, respectively.

The I_3^- or IO_3^- removal efficiency (R/%) of each adsorbent was determined using the following equation:

$$R = \frac{C_0 - C_t}{C_0} \times 100\% \quad (1)$$

where C_0 (mg/L) and C_t (mg/L) are the concentrations of I_3^- or IO_3^- before and after adsorption, respectively.

The separation efficiency (SE/%) for I_3^- and IO_3^- of each adsorbent was determined using the following equation:

$$SE(\%) = \frac{\Delta C_{t,1} - \Delta C_{t,2}}{C_{0,1}} \times 100\% \quad (2)$$

where $\Delta C_{t,1}$ (mg/L) and $\Delta C_{t,2}$ (mg/L) are the concentration change value of I_3^- and IO_3^-, $C_{0,1}$ is the initial concentration of I_3^-.

Other experimental details are provided in the Supporting Information online.

3 Results and discussion

3.1 *In-situ* synthesis of Co-LDH-R (R = Br^-, NO_3^-, and ClO_4^-) and characterization

Figure 1a shows the *in-situ* synthetic strategy used to prepare the Co-LDH-R (R = Br^-, NO_3^-, and ClO_4^-) adsorbents. Initially, ZIF-67 nanocrystals were synthesized at room temperature using cobalt ions as the metallic node and 2-methyl imidazole as the organic linker (Figure S1, Supporting Information online). Scanning electron microscopy (SEM) revealed a uniform dodecahedral morphology with an average particle size of ~500 nm (Figure S2). Subsequently, the ZIF-67 nanocrystals were refluxed in the presence of $Co(NO_3)_2\cdot 6H_2O$ in a mixed deionized water/ethanol solution at 90 °C for 5 h, yielding a green powder denoted as Co-LDH-NO_3^- (Figure S3). This process incorporates Co^{3+} in the LDH nanosheets and NO_3^- anions in the LDH interlayers. Powder X-ray diffraction (PXRD) revealed the complete disappearance of ZIF-67 and the formation of a hydrotalcite-like LDH phase [PDF#48−0601] (Figure 2a). The diffraction peaks at 2θ values of 10.35°, 19.82°, 33.89°, and 60.01° were readily indexed to (003), (006), (101), and (110) reflections of an LDH phase. The calculated (003) crystal plane spacing and the host crystallographic thickness of Co-LDH-NO_3^- were ~8.53 and ~3.84 Å, respectively, according to Bragg's equation and Materials Studio simulations (Table S1, Figure S4, Supporting Information online). The basal spacing of Co-LDH-NO_3^- was thus determined to be ~4.69 Å, with the NO_3^- inserted between the 2D sheets (Figure 2b). The SEM image of the Co-LDH-NO_3^- exhibited a typical ruffled sheet morphology (Figure 2c). Transmission electron microscopy (TEM) further confirmed the sheet-like morphology of Co-LDH-NO_3^- (Figure 2d). The corresponding energy dispersive X-ray spectroscopy (EDS) mapping images showed a uniform distribution of Co, O, and N through the na-

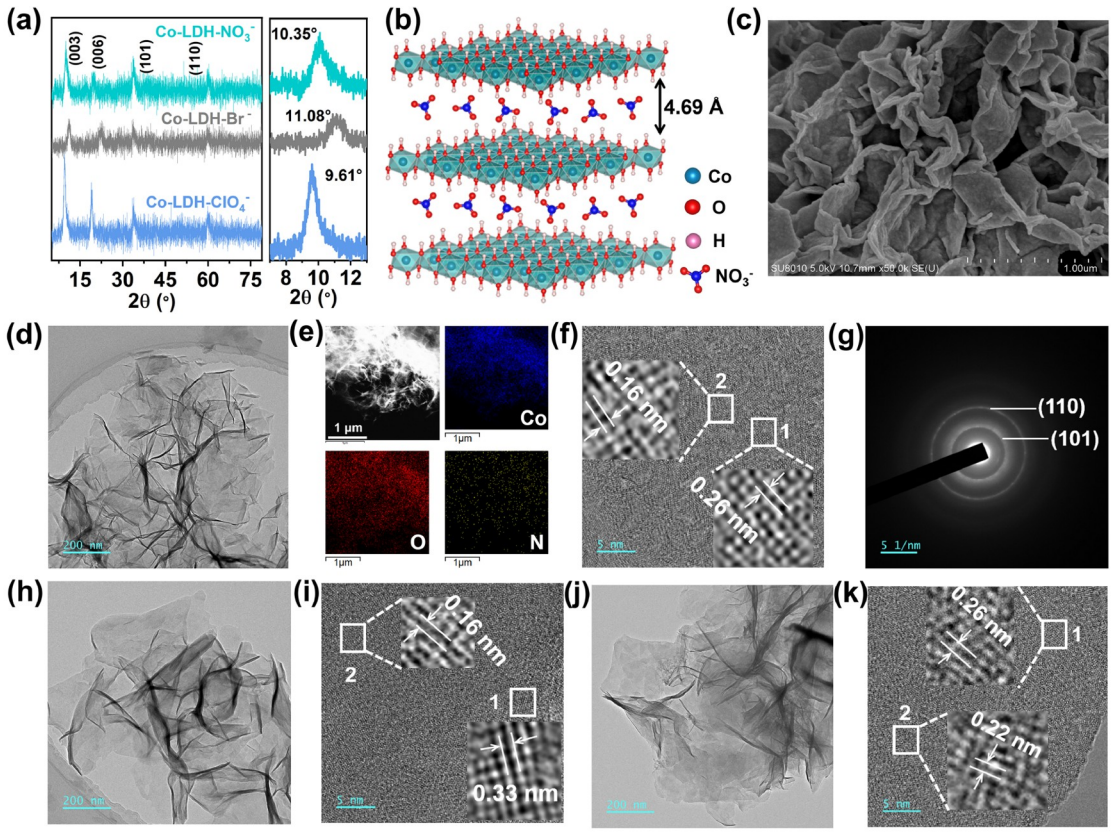

Figure 2 (Color online) (a) PXRD patterns of Co-LDH-Br^-, Co-LDH-NO_3^-, and Co-LDH-ClO_4^-. (b) The crystal structure of Co-LDH-NO_3^-. (c) SEM image of Co-LDH-NO_3^-. (d) TEM image of Co-LDH-NO_3^-. (e) HAADF-STEM and corresponding EDS images of Co-LDH-NO_3^-. (f, g) HRTEM image and SAED pattern of Co-LDH-NO_3^-. (h, i) TEM and HRTEM images of Co-LDH-Br^-. (j, k) TEM and HRTEM images of Co-LDH-ClO_4^-.

nosheets (Figure 2e). High-resolution transmission electron microscopy (HRTEM) imaging revealed lattice spacings of 0.26 and 0.16 nm for Co-LDH-NO_3^- (Figure 2f), corresponding to the selected area electron diffraction (SAED) pattern rings (Figure 2g) that could be indexed to the (101) and (110) planes of hydrotalcite-like LDH (PDF#48-0601), consistent with the PXRD results (Figure 2a).

The *in-situ* synthetic method was further extended to prepare Co-LDH-Br^- and Co-LDH-ClO_4^- under similar approaches, by replacing $Co(NO_3)_2{\cdot}6H_2O$ with $Co(ClO_4)_2{\cdot}6H_2O$ and $CoBr_2{\cdot}xH_2O$, respectively (Figure 1a and Figure S4). PXRD revealed that the (003), (006), (101), and (110) plane reflections of Co-LDH-Br^- shifted to higher 2θ values compared to Co-LDH-NO_3^-, whilst the same reflection for Co-LDH-ClO_4^- were shifted to lower 2θ values compared to Co-LDH-NO_3^-, suggesting that the basal spacing become smaller and larger, respectively. The basal spacings for Co-LDH-Br^- and Co-LDH-ClO_4^- were theoretically calculated to be 4.06 and 5.36 Å, respectively (Table S1, Figures S4–S6). SEM and TEM images revealed the expected nanosheet morphologies for Co-LDH-Br^- and Co-LDH-ClO_4^- (Figure 2h, j, Figure S7). HRTEM images for Co-LDH-Br^- showed lattice spacings of 0.33 and 0.16 nm corresponding to the PXRD (006) and (110) planes, respectively. Lattice fringes for Co-LDH-ClO_4^- at 0.26 and 0.22 nm matched the (101) (~33.89°) and (0010) planes (~39.1°), respectively. Excellent accord was found between the experimental and theoretically calculated crystallographic data (Figure 2a, i, k, Table S1).

To further study the cobalt valence state in Co-LDH-R (R = Br^-, NO_3^-, and ClO_4^-), X-ray photoelectron spectroscopy (XPS) measurements were carried out. The XPS spectra of Co-LDH-NO_3^-, Co-LDH-Br^-, and Co-LDH-ClO_4^- showed the presence of C/N/O/Co, C/O/Co/Br, and C/O/Co/Cl, respectively, consistent with their EDS mapping results (Figure 3a). The Co 2p spectra showed three sets of peaks (each in a 2:1 area ratio) associated with Co^{3+} ($2p_{3/2}$ = 780.5 eV, $2p_{1/2}$ = 796.3 eV), Co^{2+} ($2p_{3/2}$ = 781.6 eV, $2p_{1/2}$ = 797.4 eV) and cobalt "shake-up" satellites ($2p_{3/2}$ = 785.2 eV, $2p_{1/2}$ = 803.2 eV (Figure 3b) [52–54]. These results revealed the coexistence of Co^{2+} and Co^{3+} in the three Co-LDH-R samples, as expected for LDH materials which have divalent and trivalent cation sites. Thermogravimetric analysis (TGA) was used to determine the water content in Co-LDH-R (R = Br^-, NO_3^-, and ClO_4^-) [55–57]. All three samples lost interlayer water below 200 °C, allowing the number of water molecules per unit cell for Co-LDH-NO_3^-, Co-LDH-Br^-, and

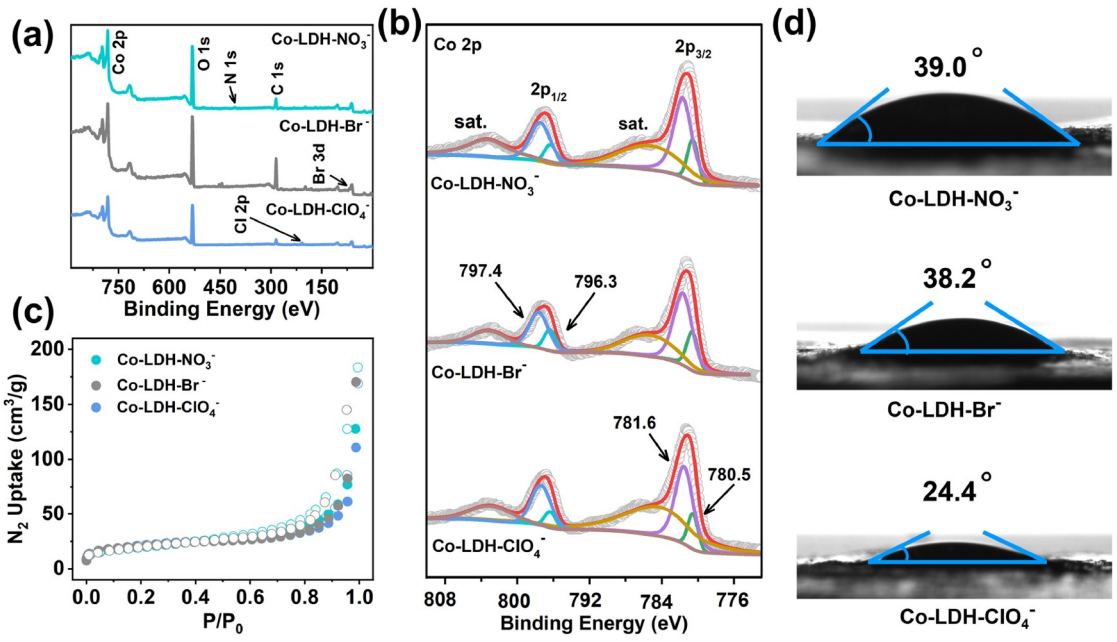

Figure 3 (Color online) (a) XPS survey spectra for Co-LDH-Br^-, Co-LDH-NO_3^-, and Co-LDH-ClO_4^-. (b) Co 2p XPS spectra for Co-LDH-NO_3^-, Co-LDH-Br^-, and Co-LDH-ClO_4^-. (c) N_2 sorption isotherms for Co-LDH-NO_3^-, Co-LDH-Br^-, and Co-LDH-ClO_4^-. (d) Contact angles for a water droplet on pressed pellets of Co-LDH-NO_3^-, Co-LDH-Br^-, and Co-LDH-ClO_4^-.

Co-LDH-ClO_4^- to be calculated as 4.3, 4.6, and 4.0, respectively (Figure S8). On the basis of XPS and TGA results, a probable general formula for the Co-LDH-R samples (R = Br^-, NO_3^-, and ClO_4^-) could be proposed: $Co^{2+}_{0.68}Co^{3+}_{0.32}(OH)_2\cdot(R^-)_{0.32}\cdot xH_2O$.

3.2 Physical and chemical properties of Co-LDH-R (R = Br^-, NO_3^-, and ClO_4^-)

N_2 adsorption-desorption isotherms were collected at 77 K to determine the porosity of Co-LDH-R (R = Br^-, NO_3^-, and ClO_4^-) (Figure 3c). The Brunauer-Emmett-Teller (BET) surface areas of Co-LDH-NO_3^-, Co-LDH-Br^-, and Co-LDH-ClO_4^- were determined to be 68.6, 69.1, and 73.4 m^2/g, respectively. Water contact angle experiments were next conducted to probe the surface wettability of Co-LDH-R (R = Br^-, NO_3^-, and ClO_4^-). Water contact angles were 39.0°, 38.2°, and 24.4° for Co-LDH-NO_3^-, Co-LDH-Br^-, and Co-LDH-ClO_4^-, respectively, suggesting considerable hydrophilicity and easy dispersibility in aqueous solutions (Figure 3d).

In view of the above structural and physical properties, we hypothesized that the *in-situ* synthesized LDH sorbents should offer vastly differing properties for separating I_3^- and IO_3^- anions from aqueous solutions. As a proof-of-concept, we carried out I_3^-/IO_3^- sorption and separation experiments to evaluate the selective adsorption abilities of the Co-LDH-R (R = Br^-, NO_3^-, and ClO_4^-) adsorbents. Our experimental findings below fully validate our hypothesis.

3.3 I_3^- and IO_3^- adsorption and separation performance

In preliminary experiments, we determined that an adsorbent-to-liquid ratio of 0.4 g/L was suitable for each Co-LDH-R (R = Br^-, NO_3^-, and ClO_4^-) sample and used this ratio in subsequent studies (Figure S9). Equilibrium adsorption data were collected with I_3^- or IO_3^- concentrations ranging from ~10 to ~200 ppm to determine the adsorption capacity of each Co-LDH-R in aqueous solutions (Figure 4a, b). Co-LDH-NO_3^- and Co-LDH-Br^- showed excellent capture capacities of 150.73 and 139.57 mg/g for I_3^-, respectively, and relatively low capture capacities of 27.56 and 16.52 mg/g for IO_3^-. However, Co-LDH-ClO_4^- with a larger window size showed high capture capacities of 165.75 and 123.8 mg/g for I_3^- and IO_3^-, respectively. Next, the adsorption kinetics of Co-LDH-R were determined in a mixed I_3^- (~10 ppm)/IO_3^- (~10 ppm) solution. As expected, Co-LDH-NO_3^- and Co-LDH-ClO_4^- demonstrated superfast I_3^- adsorption kinetics with removal ratios of >99.9% in 30 s (Figure 4c). In comparison, Co-LDH-Br^- showed relatively slow I_3^- adsorption kinetics under the same conditions (Figure 4c). This is due to Co-LDH-Br^- having the smallest basal spacing among the three Co-LDH-R samples. Notably, Co-LDH-NO_3^- and Co-LDH-Br^- did not adsorb IO_3^- in the mixed solution, whilst the adsorption ratio of Co-LDH-ClO_4 was 44% for IO_3^- in the I_3^-/IO_3^- mixture after 60 min (Figure 4c). The separation efficiency of I_3^- over IO_3^- reached ~100% in 10 s for Co-LDH-NO_3^- (Figure 4d). Co-LDH-Br^-

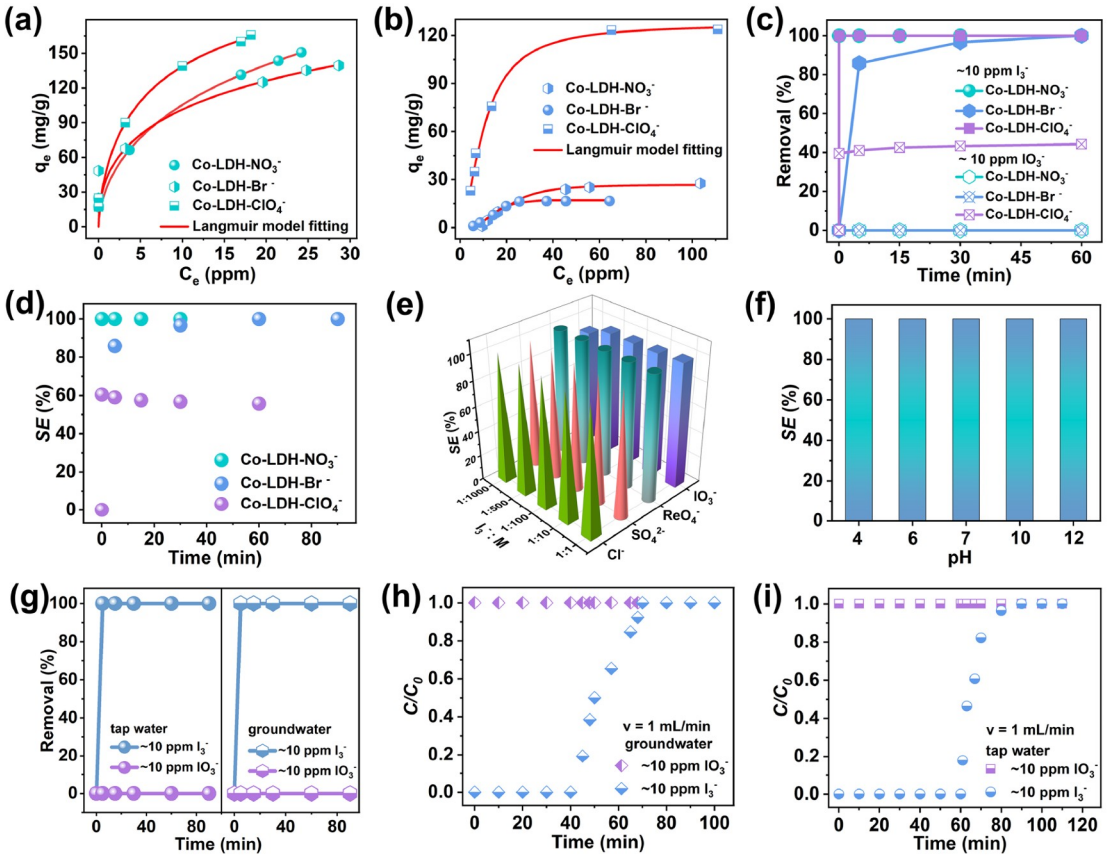

Figure 4 (Color online) (a) Equilibrium adsorption isotherms for I_3^- on Co-LDH-NO_3^-, Co-LDH-Br^-, and Co-LDH-ClO_4^- in I_3^-/IO_3^- aqueous solutions. (b) Equilibrium adsorption isotherms for of IO_3^- on Co-LDH-NO_3^-, Co-LDH-Br^-, and Co-LDH-ClO_4^- in I_3^-/IO_3^- aqueous solutions. (c) I_3^- and IO_3^- adsorption kinetics on Co-LDH-NO_3^-, Co-LDH-Br^-, and Co-LDH-ClO_4^- in a solution containing both I_3^- (~10 ppm) and IO_3^- (~10 ppm). (d) The calculated SE I_3^-/IO_3^- for Co-LDH-NO_3^-, Co-LDH-Br^-, and Co-LDH-ClO_4^-. (e) Effect of possible competing anions on I_3^- uptake by Co-LDH-NO_3^-. (f) Effect of initial pH on the removal of I_3^- by Co-LDH-NO_3^-. (g) I_3^- and IO_3^- adsorption kinetics on Co-LDH-NO_3^- in tap water and groundwater containing both I_3^- (~10 ppm) and IO_3^- (~10 ppm). (h, i) Experimental column breakthrough curves for separation of I_3^-/IO_3^- in groundwater and tap water in an absorber bed packed with Co-LDH-NO_3^-. The experimental data in Figure a–g was obtained by averaging three parallel measurements.

also showed ~100% separation efficiency but required 60 min. The highest separation efficiency for Co-LDH-ClO_4^- was 58.9% in 5 min, which decreased with increasing equilibrium time. The selective I_3^- adsorption abilities of Co-LDH-NO_3^- in the presence of various competing anions such as IO_3^-, Cl^-, SO_4^{2-}, and ReO_4^- were determined under high ionic strength conditions (Figure 4e). The relative I_3^- removal efficiency was 98.8%, 97.7%, 97.4%, 97.1%, and 90.0% at IO_3^-/I_3^- molar ratios of 1:1, 10:1, 100:1, 500:1, and 1,000:1, respectively. Further studies revealed Co-LDH-NO_3^- also showed excellent selectivity separation efficiency for I_3^- and IO_3^- in the presence of high concentrations of other anions (such as Cl^-, SO_4^{2-}, ReO_4^-), even when the other anions were in a 1,000-fold concentration relative to I_3^- (Figure 4e). Next, the I_3^-/IO_3^- separation performance of Co-LDH-NO_3^- was investigated at pH values ranging from 4 to 12 (Figure 4f). The I_3^- removal efficiency of Co-LDH-NO_3^- remained at ~100% at pH values between 4 and 12, suggesting excellent selectivity under acidic and basic conditions. The high adsorption capacity, fast kinetics, and high selectivity of Co-LDH-NO_3^- towards I_3^- over IO_3^- under various conditions prompted us to further study the dynamic separation of I_3^-/IO_3^- from contaminated water sources using Co-LDH-NO_3^- packed columns.

Iodine (including ^{127}I, ^{129}I, and ^{131}I) contamination is generally present in the form of I_3^- and IO_3^- in groundwater, where it poses a serious threat to animals and humans. Encouraged by the excellent static adsorption and separation performance of Co-LDH-NO_3^-, dynamic I_3^-/IO_3^- separation breakthrough experiments using spiked groundwater and tap water were conducted to simulate the treatment of contaminated water sources. Initially, adsorption kinetics of I_3^- and IO_3^- uptake on Co-LDH-NO_3^- in contaminated groundwater and tap water were studied at 25 °C. As expected, Co-LDH-NO_3^- exhibited fast I_3^- uptake kinetics, reaching adsorption equilibrium within 5 min in contaminated groundwater and tap water (Figure 4g). No IO_3^- adsorption was observed, suggesting extremely fast separation efficiencies in contaminated groundwater and tap water. Equilibrium adsorption results demonstrated that Co-LDH-

NO_3^- showed excellent uptake capacities of 119.94 and 127.18 mg/g for I_3^- in I_3^-/IO_3^- contaminated groundwater and tap water, respectively, and very low capture capacities of IO_3^- (Figure S10). Co-LDH-NO_3^- further showed outstanding separation performance and good durability in contaminated groundwater and tap water, with separation efficiencies maintained at ~100% after five cycles (Figure S11). This good performance is attributed to the "special memory effect" shown by LDHs during the cyclic separation of I_3^- and IO_3^- (Figure S12), that is, the interlayer channel will contract/enlarge slightly as necessary during adsorption-desorption cycles [58,59]. After the cycling tests, SEM images showed that Co-LDH-NO_3^- retained its initial morphology and crystal structure, implying excellent structural stability (Figure S13). Next, we examined the dynamic separation performance for IO_3^- and I_3^- of Co-LDH-NO_3^- through breakthrough experiments (Figure 4h, i). As shown in Figure 4h, Co-LDH-NO_3^- can effectively capture I_3^- from I_3^-/IO_3^- spiked groundwater under 1 mL/min column elution conditions, reaching equilibrium after ~40 min, while the IO_3^- was rapidly eluted through the column. The calculated dynamic adsorption capacity for I_3^- reached 15.3 mg/g. The breakthrough time for I_3^- in tap water using Co-LDH-NO_3^- was approximately ~60 min, with the equilibrium dynamic capacity being 17.6 mg/g (Figure 4i). The lower equilibrium dynamic capacity in groundwater is due to the higher ionic strength and more complex composition of groundwater compared to tap water. Notably, the anion exchange process was completely reversible, with the adsorbed I_3^- being easily eluted using 30 ppm $NaNO_3$ solutions with negligible subsequent changes in I_3^- uptake. The total column sorption capacity remained unchanged for all four runs of adsorption/elution (Figure S14). These results revealed that Co-LDH-NO_3^- could efficiently capture I_3^- to yield pure IO_3^- solutions under dynamic conditions. The long breakthrough time, high dynamic capacity, and reusability suggest that Co-LDH-NO_3^- is a very promising adsorbent for use in packed columns to capture and separate iodide from contaminated water sources.

3.4 Mechanism studies

After demonstrating the excellent IO_3^- and I_3^- separation performance, the I_3^- and IO_3^- separation mechanism was investigated using experimental approaches and theoretical calculations. The XPS spectra of used Co-LDH-NO_3^- showed the disappearance of the N signal for interlayer nitrate, together with the appearance of I signals, indicating complete anionic exchange replacement of NO_3^- by I_3^- (Figure 5a). The I 3d XPS spectrum showed peaks at 618.8 and 630.3 eV in the 3:2 area ratio, corresponding to the I $3d_{5/2}$ and I $3d_{3/2}$ peaks, respectively, of I_3^- (Figure 5b) [60,61]. No IO_3^- signals were detected. XPS analysis of Co-LDH-ClO_4^- after the adsorption experiments in I_3^-/IO_3^- showed peaks due to I_3^- and IO_3^- species (the latter having I $3d_{5/2}$ = 624.0 eV and I $3d_{3/2}$ = 635.5 eV) [62], indicating both I_3^- and IO_3^- were adsorbed in the interlayer of Co-LDH-ClO_4^-, consistent with the aforementioned adsorption results (Figure 5c). Compared with the Co 2p XPS spectra for the initial Co-LDH-NO_3^- material, the Co $2p_{3/2}$ and Co $2p_{1/2}$ signals were shifted to lower binding energy by 0.7 eV after the adsorption I_3^- (Figure 5d), which is attributed to the transfer of electron density from I_3^- to Co, suggesting the strong interaction between the LDH host and I_3^- guest. Similar results were obtained for Co-LDH-Br^- and Co-LDH-ClO_4^- after I_3^-/IO_3^- adsorption studies, further confirming strong "host-guest" interaction forces between the LDHs and I_3^-/IO_3^- (Figures S15 and S16).

Subsequently, we investigated the ion exchange behavior between interlayer anions of the LDHs and I_3^- ions in solution using *ab initio* molecule dynamics (AIMD) simulations. The ion exchange of interlayer NO_3^- by I_3^- was visualized through the simulations. As shown in Figure 5e, after immersion in an aqueous solution containing I_3^- and IO_3^- anion, the interlayer region (8.53 Å) of Co-LDH-NO_3^- contains I_3^-, NO_3^-, and H_2O molecules, with no uptake of the larger sized IO_3^- (Figure 5e, 0 ps). I_3^- in the interlayer of Co-LDH-NO_3^- migrates toward the positively charged LDHs host layers, subsequently, electrostatic interactions between I_3^- and LDH host layers are formed (as was seen by XPS). After ~3.0 ps, the exchange process between NO_3^- and I_3^- reaches equilibrium. The NO_3^- gradually moved away from the LDH host and entered the surrounding solution. The distance between the I_3^- ions and the LDH host layer is ~4.86 Å. However, the distance between I_3^- and NO_3^- is 14.0 Å, confirming that the ion exchange process is complete (Figure 5e, f). The ions exchange processes of I_3^- replacing Br^- in the interlayer of Co-LDH-Br^- and I_3^-/IO_3^- replacing ClO_4^- in the interlayer of Co-LDH-ClO_4^- were similar to those discussed above except that Co-LDH-ClO_4^- adsorbed both I_3^- and IO_3^- (Figure 5g, h, Figures S17 and S18). The ion exchange equilibrium times are 3.3 and 4.0 ps for Co-LDH-Br^- and Co-LDH-ClO_4^-, respectively, slower than that of Co-LDH-NO_3^- (3.0 ps). Moreover, Co-LDH-NO_3^- possesses the shortest Co-LDH-$NO_3^-\cdots I_3^-$ distance of 4.86 Å, indicating a stronger host-guest interaction. Distances for Co-LDH-$Br^-\cdots I_3^-$ and Co-LDH-$ClO_4^-\cdots I_3^-$ were 5.01 and 10.74 Å, respectively. Taken together, Co-LDH-NO_3^- showed the fastest separation kinetics for I_3^-/IO_3^- from the AIMD simulations, consistent with the experimental results.

On the basis of the above results, we verified that our strategy for achieving efficient separation of I_3^- and IO_3^- from aqueous solution by tuning the LDH basal spacing to allow selective anion (I_3^-) intercalation. Since Co-LDH-NO_3^- possessed a layer spacing that perfectly matched the I_3^- size and excluded the larger IO_3^-, as well as strong "host-

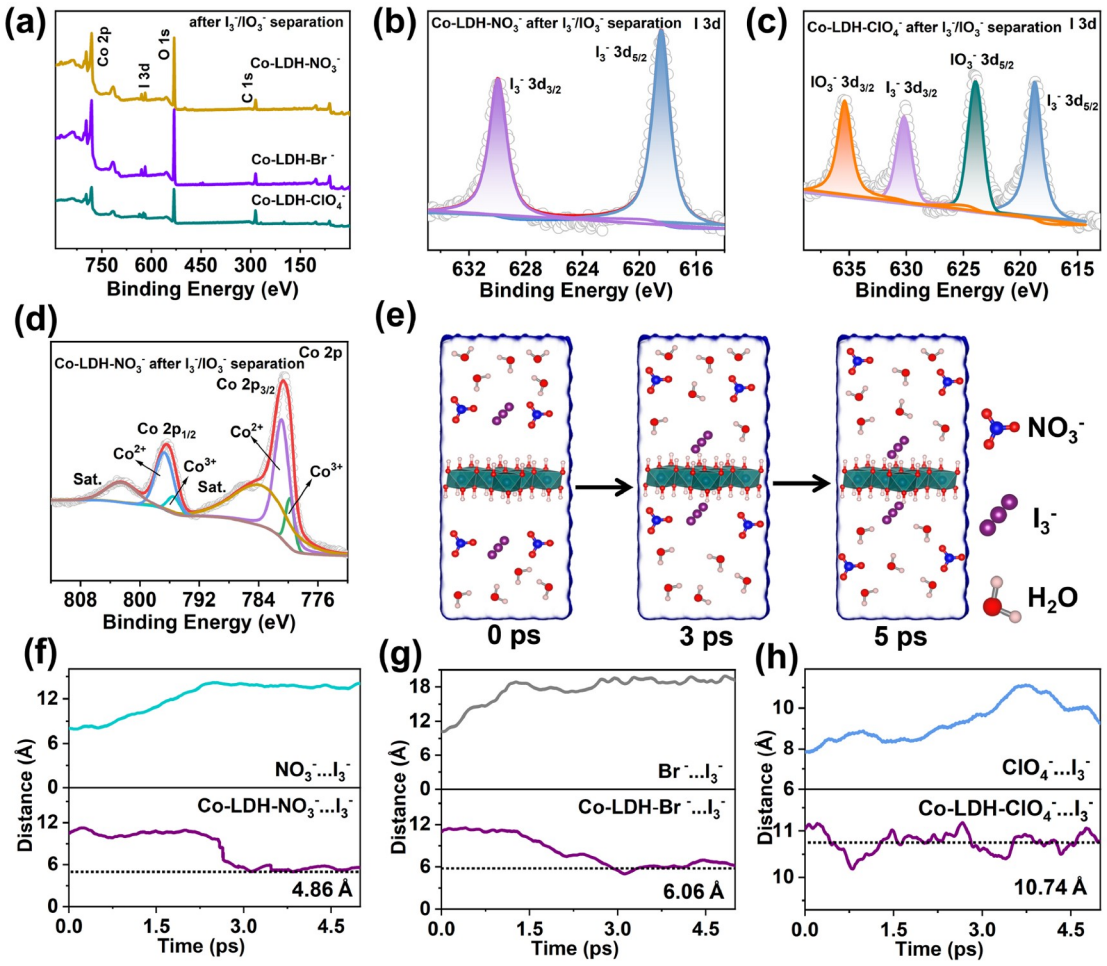

Figure 5 (Color online) (a) XPS survey spectra for Co-LDH-NO_3^-, Co-LDH-Br^-, and Co-LDH-ClO_4^- after I_3^-/IO_3^- separation studies. (b, c) I 3d XPS spectra for Co-LDH-NO_3^- and Co-LDH-ClO_4^- after I_3^-/IO_3^- separation studies. (d) Co 2p XPS spectrum for Co-LDH-NO_3^- after I_3^-/IO_3^- separation studies. (e) Selected snapshots from the molecular dynamics simulation showing the anion exchange process (I_3^-) on Co-LDH-NO_3^- in aqueous solutions. Time evolution of the distance between the Co-LDH-$NO_3^-\cdots I_3^-$ and $NO_3^-\cdots I_3^-$ (f), Co-LDH-$Br^-\cdots I_3^-$ and $Br^-\cdots I_3^-$ (g), Co-LDH-$ClO_4^-\cdots I_3^-$ and $ClO_4^-\cdots I_3^-$ (h).

guest" interaction forces between LDH and I_3^-, it showed extremely fast separation rates and very high selectivity under various conditions. It is worth mentioning that the interlayer spacing of Co-LDH-NO_3^- can be self-adjusted to the optimal value within a certain range to accommodate I_3^- whilst maintaining a strong binding affinity. Co-LDH-Br^- with a smaller window size exhibited slower kinetics for the separation of I_3^- and IO_3^-. Co-LDH-ClO_4^- with larger layer spacing showed poor I_3^-/IO_3^- separation efficiency. Moreover, the preparation of Co-LDH-NO_3^- could be easily scaled to 10.1 g in the laboratory (Figure S19), suggesting the potential for even larger-scale (kg or t scale) production and application.

4 Conclusions

In this work, a family of cobalt-based layered double hydroxides was rationally designed for the separation of I_3^-/IO_3^- in aqueous solutions. A Co-LDH-NO_3^- adsorbent with interlayer nitrate ions had an optimal interlayer spacing of ~4.69 Å, allowing selective removal of I_3^- from aqueous solutions by anion exchange (I_3^- replacing interlayer NO_3^-). Owing to the strong "host (LDH)-guest (I_3^-)" interaction forces, Co-LDH-NO_3^- exhibited super-fast and ~100% I_3^-/IO_3^- separation efficiency under various conditions (IO_3^- being larger could not be accommodated in the Co-LDH-NO_3^- interlayer). Co-LDH-NO_3^- showed excellent performance for the dynamic separation of I_3^-/IO_3^- from contaminated groundwater and tap water. Moreover, the excellent separation properties of Co-LDH-NO_3^- for I_3^-/IO_3^-, together with ease of large-scale preparation, suggest the feasibility of Co-LDH-NO_3^- for practical use. Taken together, our strategy of achieving rapid separation of I_3^-/IO_3^- by tuning the basal spacing in LDH materials provides a new platform for the management of iodine pollutants in water sources, whilst offering an approach for the separation and extraction of other anionic contaminants in water.

Acknowledgements This work was supported by the National Natural Science Foundation of China (22322603, U2167218, U2067215), the Beijing Outstanding Young Scientist Program. G.I.N.W. acknowledges funding support from the MacDiarmid Institute for Advanced Materials and Nanotechnology. S. M. acknowledges the Robert A. Welch Foundation (B-0027).

Conflict of interest The authors declare no conflict of interest.

Supporting information The supporting information is available online at chem.scichina.com and link.springer.com/journal/11426. The supporting materials are published as submitted, without typesetting or editing. The responsibility for scientific accuracy and content remains entirely with the authors.

1 Küpper FC, Feiters MC, Olofsson B, Kaiho T, Yanagida S, Zimmermann MB, Carpenter LJ, Luther Iii GW, Lu Z, Jonsson M, Kloo L. *Angew Chem Int Ed*, 2011, 50: 11598–11620
2 Rakoczy R, Kopeć A, Piątkowska E, Smoleń S, Skoczylas Ł, Leszczyńska T, Sady W. *Biol Trace Elem Res*, 2016, 174: 347–355
3 Metrangolo P, Resnati G. *Nat Chem*, 2011, 3: 260
4 Miles EA, Vahlberg T, Calder PC, Houttu N, Pajunen L, Koivuniemi E, Mokkala K, Laitinen K. *Eur J Nutr*, 2022, 61: 2919–2927
5 Beals DM, Hayes DW. *Sci Total Environ*, 1995, 173-174: 101–115
6 Riley BJ, Vienna JD, Strachan DM, McCloy JS, Jerden Jr. JL. *J Nucl Mater*, 2016, 470: 307–326
7 Guo Q, Li J, Zhao Y, Li L, He L, Zhao F, Zhai F, Zhang M, Chen L, Chai Z, Wang S. *Angew Chem Int Ed*, 2024, 63: e202400849
8 Suess E, Aemisegger F, Sonke JE, Sprenger M, Wernli H, Winkel LHE. *Environ Sci Technol*, 2019, 53: 1905–1917
9 Saiz-Lopez A, Plane JMC, Baker AR, Carpenter LJ, von Glasow R, Gómez Martín JC, McFiggans G, Saunders RW. *Chem Rev*, 2012, 112: 1773–1804
10 Kolb CE. *Nature*, 2002, 417: 597–598
11 Zhang Y, He L, Pan T, Xie J, Wu F, Dong X, Wang X, Chen L, Gong S, Liu W, Kang L, Chen J, Chen L, Chen L, Han Y, Wang S. *CCS Chem*, 2022, 5: 1540–1548
12 Han W, Clarke W, Pratt S. *Ecol Eng*, 2016, 94: 286–294
13 Liu X, Zhang Z, Shui F, Zhang S, Li L, Wang J, Yi M, You Z, Yang S, Yang R, Wang S, Liu Y, Zhao Q, Li B, Bu X, Ma S. *Angew Chem Int Ed*, 2024, 63: e202411342
14 Gao M, Chen W, Sun H, Fan L, Wang W, Du C, Chen Y, Lin L, Pearce EN, Shen J, Cheng Y, Wang C, Zhang W. *Nutr Res*, 2019, 66: 61–67
15 He L, Chen L, Dong X, Zhang S, Zhang M, Dai X, Liu X, Lin P, Li K, Chen C, Pan T, Ma F, Chen J, Yuan M, Zhang Y, Chen L, Zhou R, Han Y, Chai Z, Wang S. *Chem*, 2021, 7: 699–714
16 Xu S, Zhang L, Freeman SPHT, Hou X, Shibata Y, Sanderson D, Cresswell A, Doi T, Tanaka A. *Environ Sci Technol*, 2015, 49: 1017–1024
17 Tai B, Li B, He L, Ma Z, Lin S, Zhang M, Chen J, Wu F, Chen L, Dai X, Ma F, Chai Z, Wang S. *Sci China Chem*, 2024, 67: 1569–1577
18 Patil SA, Rodríguez-Berríos RR, Chavez-Flores D, Wagle DV, Bugarin A. *ACS EST Water*, 2023, 3: 2009–2023
19 Balter M. *Science*, 1995, 270: 1758–1759
20 Jeong H, Lee DW, Hong SJ, Kim J, Kim M, Kim J, Lee HS, Park TH, Kim HK, Park JI, Kim JY, Lim SH, Hyeon T, Han B, Bae SE. *Water Res*, 2022, 222: 118864
21 Tachibana Y, Kalak T, Nogami M, Tanaka M. *Water Res*, 2020, 182: 116032
22 Duborská E, Urík M, Kubová J. *Arch Agronomy Soil Sci*, 2018, 64: 46–57
23 Chen D, Ma T, Zhao X, Jing X, Zhao R, Zhu G. *ACS Appl Mater Interfaces*, 2022, 14: 47126–47135
24 Farebrother J, Zimmermann MB, Andersson M. *Ann New York Acad Sci*, 2019, 1446: 44–65
25 Bichsel Y, von Gunten U. *Environ Sci Technol*, 1999, 33: 4040–4045
26 Moran JE, Oktay SD, Santschi PH. *Water Resour Res*, 2002, 38: 24
27 Kim TJ, Kim M, Jung SH, Yeon JW. *J Radioanal Nucl Chem*, 2018, 316: 1267–1272
28 Liu H, Li J, Cao H, Xie X, Wang Y. *J Environ Manage*, 2022, 303: 114249
29 Fuge R, Johnson CC. *Environ Geochem Health*, 1986, 8: 31–54
30 Bellido AV Jr. *J Radioanal Nucl Chem*, 2001, 249: 653–656
31 Cox EM, Arai Y. *Adv Agron*, 2014, 128: 47–96
32 Jin K, Lee B, Park J. *Coord Chem Rev*, 2021, 427: 213473
33 Pan H, Li B, Yang J, Liu W, Luo W, Chen B. *J Hazard Mater*, 2023, 460: 132423
34 Kaufhold S, Pohlmann-Lortz M, Dohrmann R, Nüesch R. *Appl Clay Sci*, 2007, 35: 39–46
35 Hoskins JS, Karanfil T, Serkiz SM. *Environ Sci Technol*, 2002, 36: 784–789
36 Zhang X, Gu P, Li X, Zhang G. *Chem Eng J*, 2017, 322: 129–139
37 Chapman KW, Chupas PJ, Nenoff TM. *J Am Chem Soc*, 2010, 132: 8897–8899
38 Xie L, Zheng Z, Lin Q, Zhou H, Ji X, Sessler JL, Wang H. *Angew Chem Int Ed*, 2022, 61: e202113724
39 Lin Y, Jiang X, Kim ST, Alahakoon SB, Hou X, Zhang Z, Thompson CM, Smaldone RA, Ke C. *J Am Chem Soc*, 2017, 139: 7172–7175
40 Liu YJ, Sun YF, Shen SH, Wang ST, Liu ZH, Fang WH, Wright DS, Zhang J. *Nat Commun*, 2022, 13: 6632
41 Dai D, Yang J, Zou Y, Wu J, Tan L, Wang Y, Li B, Lu T, Wang B, Yang Y. *Angew Chem Int Ed*, 2021, 60: 8967–8975
42 Zhang M, Samanta J, Atterberry BA, Staples R, Rossini AJ, Ke C. *Angew Chem Int Ed*, 2022, 61: e202214189
43 Yan Z, Yuan Y, Tian Y, Zhang D, Zhu G. *Angew Chem Int Ed*, 2015, 54: 12733–12737
44 Zhang X, Maddock J, Nenoff TM, Denecke MA, Yang S, Schröder M. *Chem Soc Rev*, 2022, 51: 3243–3262
45 Shi YZ, Hu QH, Gao X, Zhang L, Liang RP, Qiu JD. *Sep Purif Tech*, 2023, 312: 123366
46 Xie Y, Rong Q, Mao F, Wang S, Wu Y, Liu X, Hao M, Chen Z, Yang H, Waterhouse GIN, Ma S, Wang X. *Nat Commun*, 2024, 15: 2671
47 Hao M, Liu Y, Wu W, Wang S, Yang X, Chen Z, Tang Z, Huang Q, Wang S, Yang H, Wang X. *EnergyChem*, 2023, 5: 100101
48 Jenkins HDB, Thakur KP. *J Chem Educ*, 1979, 56: 576
49 Mantina M, Chamberlin AC, Valero R, Cramer CJ, Truhlar DG. *J Phys Chem A*, 2009, 113: 5806–5812
50 Niu Q, Yang M, Luan D, Li NW, Yu L, Lou XWD. *Angew Chem Int Ed*, 2022, 61: e202213049
51 Banerjee R, Phan A, Wang B, Knobler C, Furukawa H, O'Keeffe M, Yaghi OM. *Science*, 2008, 319: 939–943
52 Zhang SL, Guan BY, Lu XF, Xi S, Du Y, Lou XWD. *Adv Mater*, 2020, 32: 2002235
53 Yilmaz G, Yam KM, Zhang C, Fan HJ, Ho GW. *Adv Mater*, 2017, 29: 1606814
54 Tung CW, Hsu YY, Shen YP, Zheng Y, Chan TS, Sheu HS, Cheng YC, Chen HM. *Nat Commun*, 2015, 6: 8106
55 Carrasco JA, Cardona-Serra S, Clemente-Juan JM, Gaita-Ariño A, Abellán G, Coronado E. *Inorg Chem*, 2018, 57: 2013–2022
56 Iyi N, Ebina Y, Sasaki T. *Langmuir*, 2008, 24: 5591–5598
57 Dillenburger JD, Schulte L, Mahale P, Suleiman M, Mallouk TE. *Chem Mater*, 2023, 35: 6437–6446
58 Ye H, Liu S, Yu D, Zhou X, Qin L, Lai C, Qin F, Zhang M, Chen W, Chen W, Xiang L. *Coord Chem Rev*, 2022, 450: 214253
59 Gunawan P, Xu R. *Chem Mater*, 2009, 21: 781–783
60 Hao M, Xie Y, Lei M, Liu X, Chen Z, Yang H, Waterhouse GIN, Ma S, Wang X. *J Am Chem Soc*, 2024, 146: 1904–1913
61 Jiang Y, Jung H, Joo SH, Sun QK, Li C, Noh H, Oh I, Kim YJ, Kwak SK, Yoo J, Baek J. *Angew Chem Int Ed*, 2021, 60: 17191–17197
62 Wang N, Xiong R, Zhang G, Liu R, He X, Huang S, Liu H, Qu J. *Water Res*, 2022, 223: 118965